

Riemannian Denoising Score Matching for Molecular Structure Optimization with Accurate Energy

Jeheon Woo^{1†}, Seonghwan Kim^{1†}, Jun Hyeong Kim¹
and Woo Youn Kim^{1,2*}

¹Department of Chemistry, KAIST, 291 Daehak-ro, Yuseong-gu,
34141, Daejeon, Republic of Korea.

²AI Institute, KAIST, 291 Daehak-ro, Yuseong-gu, 34141,
Daejeon, Republic of Korea.

*Corresponding author(s). E-mail(s): wooyoun@kaist.ac.kr;
Contributing authors: woojh@kaist.ac.kr; dmdtka00@kaist.ac.kr;
junhkim1226@kaist.ac.kr;

[†]These authors contributed equally to this work.

Abstract

This study introduces a modified score matching method aimed at generating molecular structures with high energy accuracy. The denoising process of score matching or diffusion models mirrors molecular structure optimization, where scores act like physical force fields that guide particles toward equilibrium states. To achieve energetically accurate structures, it can be advantageous to have the score closely approximate the gradient of the actual potential energy surface. Unlike conventional methods that simply design the target score based on structural differences in Euclidean space, we propose a Riemannian score matching approach. This method represents molecular structures on a manifold defined by physics-informed internal coordinates to efficiently mimic the energy landscape, and performs noising and denoising within this space. Our method has been evaluated by refining several types of starting structures on the QM9 and GEOM datasets, demonstrating that the proposed Riemannian score matching method significantly improves the accuracy of the generated molecular structures, attaining chemical accuracy. The implications of

this study extend to various applications in computational chemistry, offering a robust tool for accurate molecular structure prediction.

Keywords: Molecular conformation, Structure optimization, Machine learning, Score matching, Diffusion model, Riemannian manifold

1 Introduction

The accurate prediction of molecular structures is pivotal in various scientific fields, ranging from drug discovery to materials science [1, 2]. Understanding the spatial arrangement of atoms within molecules not only elucidates their properties but also facilitates the design of novel compounds with desired characteristics [3, 4]. Traditionally, quantum mechanical simulations, such as density functional theory (DFT), have been the primary approach for predicting molecular structures [5, 6]. However, the inherent complexity and high computational cost of these simulations often limit their practicality, including their extension to larger systems [7–10]. This limitation presents significant challenges in extending these methods to more complex compounds, highlighting the need for more efficient and scalable predictive approaches [11–15].

In recent years, machine learning techniques have emerged as powerful tools in the field of molecular modeling, offering the potential to overcome these challenges and revolutionize structure prediction [16–18]. Previous research has demonstrated the efficacy of machine learning in predicting molecular properties and structures, paving the way for innovative applications in diverse domains. One category of molecular structure prediction involves learning the potential energy surface (PES), where models aim to predict the potential energy and associated forces of a given molecular structure [11, 16, 19–21]. These methods rely on auxiliary optimization algorithms, similar to conventional computational chemistry approaches, to find molecular structures by navigating the energy landscape. While they provide valuable insights into the energy surface, they require extensive *ab initio* computations for training data preparation.

On the other hand, generative models for molecular structure prediction have been developed to learn distributions of atomic positions directly [17, 18, 22–29]. Variational autoencoders, for example, offer one-shot generation of molecular conformers by predicting internal coordinates such as interatomic distances and angles [22, 23]. More recently, denoising score matching (DSM) based models have been developed to learn the score function, which is the gradient of the log-likelihood [24–26]. The score function points in the direction of the clean data, guiding a noisy molecular structure toward its clean form. The denoising process in DSM is analogous to conventional molecular structure optimization algorithms, where the score function acts like physical force fields, steering molecular structures toward their equilibrium states.

DSM-based approaches have achieved state-of-the-art accuracy in various conformer predictions [17, 18, 28]. Despite their promise, existing DSM methods have not yet reached chemical accuracy—typically defined as an energy error of less than 1 kcal/mol—which limits their reliability for applications requiring high precision.

To improve the energy accuracy of DSM, we propose a novel approach that combines the strengths of both score matching and PES learning models. A key challenge in structure prediction is selecting a metric that not only captures structural discrepancies but also reflects energetic relevance. Commonly used metrics, such as the L^2 norm in Euclidean space, often fall short in this regard. To address this, we adopt physics-informed internal coordinates, inspired by the geodesic interpolation method of Zhu et al. [30], which provide a better metric aligning with molecular energy differences (see Figure 1). Building on this foundation, we design the associated Riemannian manifold that closely mirrors the molecular energy landscape.

Training DSM models with Gaussian perturbation on the manifold allows the score function to more closely approximate the actual forces on the PES, enabling the model to accurately learn the distribution of molecular structures while ensuring that the generated structures are energetically precise. We conducted a comparative analysis of noisy structures sampled in both the Euclidean and Riemannian spaces, revealing a substantial divergence between the two (see Figure 2). Notably, the deviation between DFT structures and structures sampled in noisy distribution in the Riemannian space was analogous to the discrepancy observed between DFT structures and MMFF structures, implying that the Riemannian noise-sampling yields more molecular-like noisy structures.

To demonstrate the efficacy of our Riemannian DSM (R-DSM) approach, we first evaluate it on DFT structures from the QM9 dataset [31]. We conducted a comparative analysis of DSMs in Euclidean and Riemannian spaces, focusing on both structural and energy accuracy. For the accuracy evaluation against the reference DFT conformation, we used MMFF-optimized structures [32] from the QM9_M dataset [33] as starting points, derived from the reference DFT structures to maintain consistent conformations. The Riemannian model achieved state-of-the-art performance with a median energy error of 0.177 kcal/mol and a root mean square deviation (RMSD) of 0.031 Å. Furthermore, we applied our approach to the conformer generation task using the GEOM-QM9 subset of the GEOM [34] dataset, where various predicted structures from ETKDG [35] and generative models [17, 24] were used as starting points. Post-refinement using R-DSM not only improved the structure-based evaluation measurements, but also enhanced the ensemble properties, demonstrating the broad utility of our method. These results validate the effectiveness of our approach, especially in achieving high energy accuracy within chemical accuracy—an essential criterion for practical applications in molecular modeling.

2 Results

2.1 Design of physics-informed Riemannian manifold

To enhance the energy accuracy of DSM, we employed physics-informed internal coordinates to represent molecular structures, inspired by the geodesic interpolation method [30] defined as

$$q^e = \exp(-\alpha(r^e - 1)) + \beta \frac{1}{r^e}, \quad (1)$$

$$r^e = \frac{\|\mathbf{r}_i - \mathbf{r}_j\|_2}{R_i + R_j}, \quad (2)$$

where $e \in \mathcal{E}$ denotes an edge between the i -th and j -th atoms, \mathbf{r}_i represents the position vectors of the i -th atom, and R_i corresponds to the covalent radius of the i -th atom’s element. The parameters $\alpha=1.7$ and $\beta = 0.01$ are set according to Zhu et al [30].

In other words, a molecular structure can be represented as a vector $(\mathbf{r}_i)_{i=1,2,\dots,N} \in \mathbb{R}^{N \times 3}$ in Euclidean space, and alternatively as $(q^e)_{e \in \mathcal{E}} \in \mathbb{R}^{|\mathcal{E}|}$. In particular, in the case of redundant coordinates where $3N < |\mathcal{E}|$, the set of feasible molecular structures is defined as a submanifold immersed in $\mathbb{R}^{|\mathcal{E}|}$ [36]. Subsequently, the Riemannian metric tensor g_{ij} and the distance element are defined with the Einstein notation as

$$g_{ij} = \frac{\partial q^e}{\partial x^i} \frac{\partial q^e}{\partial x^j}, \quad (3)$$

$$ds^2 = g_{ij} dx^i dx^j, \quad (4)$$

where x^i and x^j are mass-weighted Cartesian coordinates of the i -th and j -th atoms, respectively. Theoretically, if g_{ij} approximates the Fukui’s metric tensor derived from the PES as

$$\frac{\partial q^e}{\partial x^i} \frac{\partial q^e}{\partial x^j} \approx \frac{\partial E}{\partial x^i} \frac{\partial E}{\partial x^j}, \quad (5)$$

the geodesic distance between two structures within the same conformational cell is closely related to their energy difference [37].

To demonstrate that the Riemannian manifold better captures the energetic properties of molecular structures, we analyzed the correlation between geodesic distances and energy differences. The geodesic distances were computed using the geodesic interpolation method. Pearson correlation coefficients were calculated to assess the relationship between energy differences and these structural discrepancies. The correlations were calculated for 1,000 randomly selected pairs of molecular structures optimized by the MMFF and DFT methods from the QM9_M dataset, whose energies were calculated by single-point DFT calculations. For comparison, we also consider the widely used measures RMSD and the mean absolute error of interatomic distances (D-MAE). The

RMSD is a measure of the Euclidean distance between corresponding atoms in two molecular structures, averaged over all atoms and given as the square root of the mean of the squared distances. On the other hand, D-MAE computes the average deviation of interatomic distances in internal coordinates. A detailed method for the measurements is given in Section 4.1.

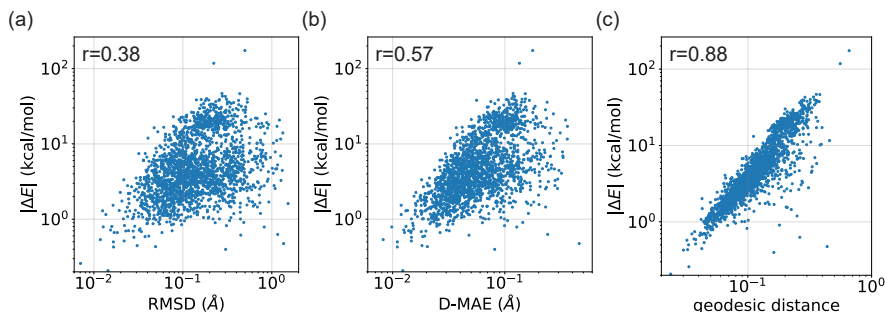


Fig. 1 Correlation of energy differences ($|\Delta E|$) with three measures of structural differences: (a) root mean square deviation (RMSD), (b) mean absolute error of interatomic distances (D-MAE), and (c) geodesic distance. The energy and structure differences were calculated for 1,000 randomly selected pairs of structures optimized by the MMFF and DFT methods. Both the x- and y-axes are plotted on a log-log scale and have been adjusted for better visualization. Pearson’s correlation coefficients (r), shown in red, quantify the linear relationship between the energy differences and each structural measurement.

Figure 1 presents a comparative analysis of the correlation between energy differences ($|\Delta E|$) and three different measures of structural differences: (a) RMSD, (b) D-MAE, and (c) geodesic distance. The Pearson correlation coefficients, denoted as “ r ” in Figure 1, indicate the strength of the linear relationship between the energy difference and each structural error. Among the three measurements, RMSD shows the lowest correlation with energy differences, suggesting that it may not adequately capture energetically relevant structural deviations. In contrast, D-MAE shows a higher correlation than RMSD, as it uses interatomic distances that can better capture changes in bond lengths and other subtle structural variations. The results demonstrate that the geodesic distance exhibits the highest correlation with energy differences among the three measurements, with a correlation value of 0.88, suggesting that this measurement is more effective at capturing energetically relevant structural deviations. These results support the hypothesis that the Riemannian manifold representation, which takes into account the physical intuition, provides a more meaningful metric for assessing molecular conformation.

2.2 Noise-sampling on Riemannian manifold

To train DSM models, noisy structures are generated by perturbing the original structures with controlled noise. In conventional DSM methods, a noisy

structure x_t is generated by adding noise to the original structure x_0 as follows

$$x_t = x_0 + \sigma_t \varepsilon_t, \quad (6)$$

where σ_t is the noise scale at time t , and $\varepsilon_t \sim \mathcal{N}(0, I) \in \mathbb{R}^{N \times 3}$ is a Gaussian noise vector. This results in noisy structures that are dispersed around x_0 in Euclidean space. On the other hand, in our approach, the noisy structures are generated by Brownian motion on the Riemannian manifold, which is approximated by

$$x_t = \exp_{x_0}(\sigma_t \varepsilon_t), \quad (7)$$

according to the Varadhan approximation [38]. Here, x_0 and $x_t \in \mathcal{M}$ and $\varepsilon_t \mathcal{N}(0, I) \in T_{x_0} \mathcal{M}$ is a tangent vector representing the direction of noise. The exponential map \exp_{x_0} transports the noise vector along the manifold’s geodesic starting from x_0 , ensuring that the noisy structures respect the underlying geometric constraints. Further details are provided in Section 4.2

To compare the noisy structure distributions obtained from two distinct spaces, we sampled 1,000 noisy structures from each space and calculated their RMSD values and energy differences relative to x_0 as a reference. Additionally, we calculated RMSD and energy differences for MMFF-optimized structures that correspond to the same conformations as x_0 , providing a comparative baseline between the sampled noisy and MMFF configurations. The σ_t values for the noise-sampling were adjusted according to a predefined scheduling scheme, with the maximum σ_t set to ensure a similar RMSD distribution to that of the MMFF-optimized structures.

Figure 2 presents a comparative analysis of molecular structures obtained from different methods: DFT, MMFF, Euclidean noise-sampling, and Riemannian noise-sampling. In Figure 2a, the molecular structures obtained from each method for three representative examples are visually compared, along with their respective RMSD and absolute energy difference ($|\Delta E|$) values relative to the reference DFT structures. Figure 2b shows the distributions of RMSD and $|\Delta E|$ for structures generated by MMFF, Riemannian noise-sampling, and Euclidean noise-sampling, using DFT structures as the reference. Each distribution is based on 1,000 randomly sampled molecules, with 23 cases excluded from the Euclidean noise-sampling due to SCF calculation failure.

The results indicate that while the RMSD distributions of Riemannian and Euclidean noise-sampling are similar, the $|\Delta E|$ distributions show a significant discrepancy. Specifically, Euclidean noise leads to structures with greater energetic instability, often involving bond formation or breaking, which is likely responsible for the SCF convergence failures. These results demonstrate that differences in structural measurements such as RMSD do not always translate directly to energy differences, aligning with the observation in Figure 1.

In contrast, interestingly, both the $|\Delta E|$ distributions of the Riemannian sampling and the MMFF show similarly small energy differences and more molecular-like noisy structures. In both cases, primary structural differences occur in the bond and dihedral angles with respect to the reference structures,

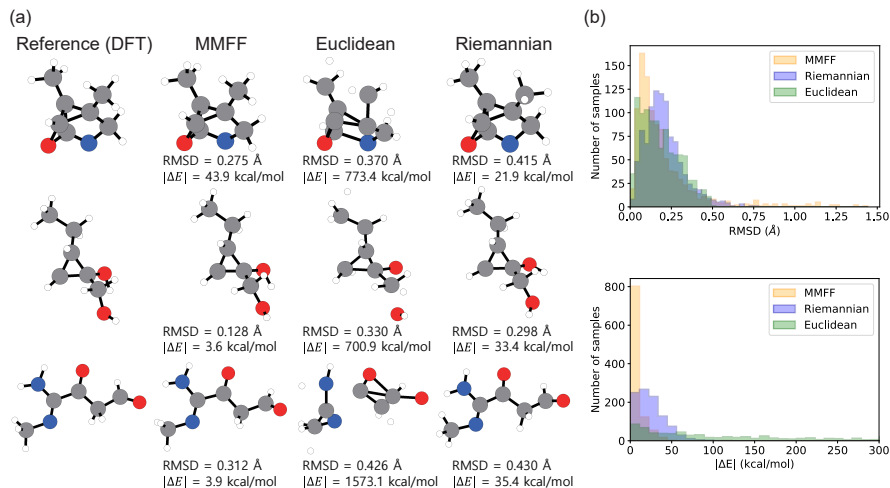


Fig. 2 Comparison of molecular structures sampled from noisy distributions of Euclidean and Riemannian spaces. **a** Visualization of obtained molecular structures: from left to right, DFT, MMFF, Euclidean noise-sampling, and Riemannian noise-sampling, with three examples visualized for each method. For each structure, the RMSD and $|\Delta E|$ values are shown with respect to the reference DFT structure. **b** The distributions of RMSD (top) and $|\Delta E|$ (bottom) for molecular structures obtained by MMFF (orange), Riemannian noise-sampling (blue), and Euclidean noise-sampling (green), with the DFT structures as reference. Each distribution is plotted with 1,000 randomly selected molecules for each method; however, 23 samples are excluded from the Euclidean noise-sampled structures due to failure to converge in the SCF calculation.

as shown in Figure 2b. Furthermore, this suggests that the structural dynamics on the Riemannian manifold defined by Eq. 3 are similar to those of molecular dynamics. More distribution results, including additional measurements, D-MAE and L^2 norm in q -coordinates, can be found in Supplementary Figure 2.

Both DSM and R-DSM are trained to denoise structures generated by Euclidean and Riemannian noise-sampling, respectively. Training details are provided in Section 4.2, which elaborates on the formulation of R-DSM through the diffusion process, the corresponding SDEs, the use of deep learning models to approximate the score function, and the loss function.

2.3 Schematic of Riemannian denoising score matching

In this section, we briefly describe the advantages of R-DSM for molecular structure optimization over DSM in Euclidean space. Figure 3a, a conceptual illustration, compares the same potential energy surface from two perspectives: Euclidean and Riemannian spaces. The green and orange lines represent the geodesic path between the equilibrium structure x_0 and its noisy structure x_t in each space, respectively, while the red lines indicate the gradient descent path for energy minimization, which corresponds to the geodesic path with respect to the Fukui’s metric tensor [37]. In the subfigures below of Figure 3a,

the direction vector from x_t to x_0 is shown on the tangent plane, and is $x_0 - x_t$ in Euclidean space and $\exp_{x_t}^{-1}(x_0)$ on Riemannian manifold, respectively. The target scores of DSM and R-DSM are simply the direction vectors scaled by $1/\sigma_t^2$.

In Euclidean space, energy level sets are distorted due to the anisotropic nature of interatomic interactions with respect to atomic Cartesian coordinates, such as bond stretching and angle bending. This distortion implies that isotropic noise on the Cartesian coordinates may result in highly unstable structures with significant energy deviations. As a result, there can be a large difference between the direction of the energy gradient and $x_0 - x_t$. In contrast, in Riemannian space equipped with the physics-informed metric, the energy level sets form nearly concentric circles around x_0 . Consequently, the energy gradient and the score function can be well aligned.

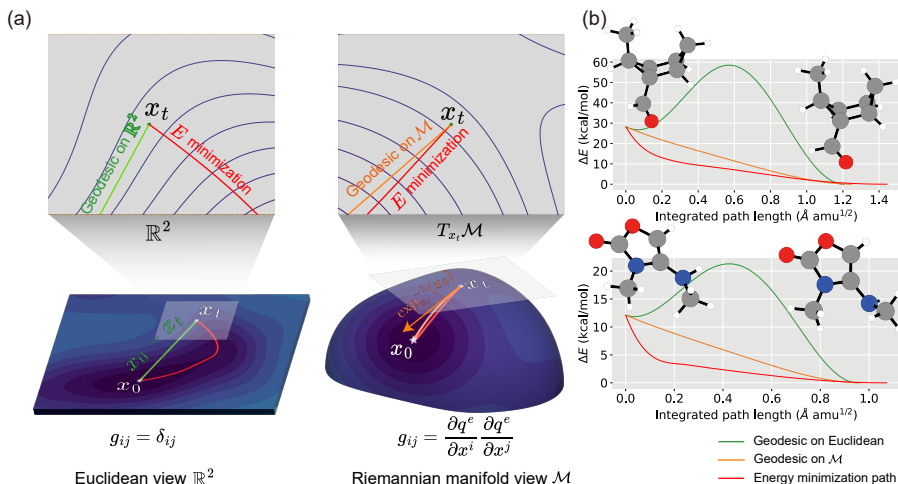


Fig. 3 Schematic of Riemannian denoising score matching (R-DSM). **a** Conceptual illustration comparing the representation of the potential energy surface (PES) in Euclidean space and the Riemannian manifold. The schematic highlights the differences between the geodesics in each space (white line) and the gradient descent path (red line) on the PES. In the subfigures below, the direction vectors for getting from x_t to x_0 , expressed on the tangent plane, are shown. **b** Energy profile comparisons between energy minimization paths (red color) and geodesics in Euclidean space (green color) the Riemannian manifold (orange color), using two examples from the QM9 dataset. The left and right endpoints correspond to the MMFF structure and the reference DFT structure, respectively.

We employ an ordinary differential equation (ODE) based sampling algorithm to utilize DSM and R-DSM models to refine sub-optimal structures to optimal structures (see Section 4.3). Given an ideal score function, ODE sampling transports the sub-optimal structure to the optimal structure along the geodesic path. In DSM, the path corresponds to the straight line, linear interpolation between sub-optimal and optimal structures in Euclidean space. To illustrate the advantage of R-DSM, Figure 3b compares the energy profiles

along the geodesic paths from MMFF to DFT structures, in Euclidean (green lines) and Riemannian spaces (orange lines), together with the energy minimization paths (red lines). The x-axis, representing the integrated path length, is calculated as the cumulative sum of the RMSD values between neighboring structures in mass-weighted Cartesian coordinates. The energy profiles of the two geodesics differ significantly, even though the integrated path lengths of the trajectories are similar. The energy profiles obtained by linear interpolation in Euclidean space are accompanied by a sharp increase in energy. In contrast, geodesics on the Riemannian manifold exhibit smooth and consistently decreasing energy profiles similar to the energy minimization paths, highlighting the potential robustness of R-DSM in molecular refinement with respect to energy.

In this regard, the introduction of Riemannian space offers advantages in modeling molecular structure in collaboration with the DSM. The score function under the Riemannian metric more closely captures the intrinsic structure associated with the energy, resembling the gradient of the potential energy surface. By adopting the physics-informed metric, the R-DSM approach accurately captures the energetics of interatomic interactions, resulting in improved performance in refining sub-optimal structures.

2.4 Performance on molecular structure prediction

First, we evaluate the performance of the R-DSM model on the QM9 dataset, with the conventional DSM serving as a baseline. To assess the precision in molecular structure predictions, MMFF structures corresponding to the same conformations as the reference molecules were used as the initial structures. Each model optimizes these structures through its predicted directions toward the reference conformations. For both the predicted structures and MMFF structures, we compare measurements that directly calculable from molecular structures, such as RMSD and D-MAE, alongside the energy difference $|\Delta E|$. These measurements are measured relative to the reference DFT structure, and $|\Delta E|$ is obtained by single-point DFT calculations.

Table 1 Comparison of RMSD, D-MAE, and $|\Delta E|$ (kcal/mol) for different models. This table shows the root mean square deviation (RMSD), the mean absolute error of the interatomic distances (D-MAE), and the energy difference ($|\Delta E|$), using the DFT structures as reference for the MMFF structures and the predicted structures by DSM and R-DSM. The evaluation was performed on the QM9 test set, and the energy values were obtained from single point DFT calculations.

	RMSD (Å)		D-MAE (Å)		$ \Delta E $ (kcal/mol)	
	Mean	Median	Mean	Median	Mean	Median
MMFF	0.200	0.137	0.0717	0.0571	7.386	4.215
DSM	0.166	0.091	0.0454	0.0280	1.560	0.816
R-DSM	0.104	0.031	0.0256	0.0095	0.806	0.177

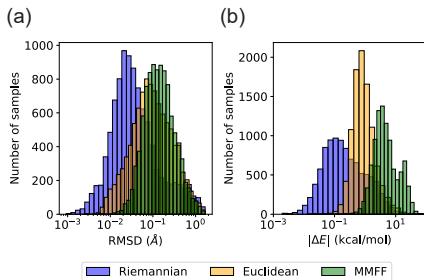


Fig. 4 Comparative analysis of molecular structures predicted by R-DSM, DSM, and MMFF. Histograms compare the distributions of (a) root mean square deviation (RMSD) and (b) absolute energy difference ($|\Delta E|$) between molecular structures predicted by R-DSM (blue) and DSM (yellow) models and MMFF (green). The sampling was performed on the QM9 test set, and the energy values were obtained from single point DFT calculations.

Table 1 presents mean and median values for each measurement across molecules in the test set, while the distributions of RMSD and $|\Delta E|$ are illustrated in Figure 4. Additional distributions, including those for D-MAE and L^2 norm on q -coordinates, can be found in Supplementary Figure 1. Notably, both DSM and R-DSM show significant improvements over the starting MMFF structures, with R-DSM achieving even greater accuracy. Comparing the median values between DSM and R-DSM reveals that while RMSD and D-MAE errors are reduced by approximately 4–5 times, $|\Delta E|$ shows an over 20-fold reduction, highlighting the substantial accuracy improvement. This remarkable reduction in $|\Delta E|$ can be attributed to R-DSM’s denoising in a space that is highly correlated with energy, enabling it to achieve better energy alignment with the reference structures. Moreover, R-DSM reaches a mean value of $|\Delta E|$ within the range of chemical accuracy, achieving an error below 1 kcal/mol, which underscores the model’s robustness in predicting molecular structure.

One advantage of the structure prediction approach, distinct from models that directly predict properties, is its allowance for post-refinement through quantum chemical calculations. This refinement process enables the attainment of optimized structures with higher accuracy. Alternatively, methods such as uncertainty quantification could also be considered for selectively refining certain structures more efficiently [28, 39].

To evaluate R-DSM in conjunction with a post refinement, we performed subsequent DFT-based optimization of the structures obtained by both MMFF and R-DSM. Table 2 presents a comparison between MMFF and R-DSM in terms of the number of force calls, SCF cycles, and SCF times. Specifically, the number of force calls indicates the iteration count of the optimization process, SCF cycles represent the total number of SCF iterations performed across all optimization steps, and SCF times reflect the total time spent on the optimization.

R-DSM achieves a marked improvement, reducing both the number of iterations and the computation time by more than twofold compared to MMFF. For the majority of cases, R-DSM converges to the final structure in only three steps, underscoring its effectiveness in the subsequent optimization process. The model inference time for R-DSM, detailed in Supplementary Table 5, is negligible compared to the overall computational savings achieved.

Table 2 Comparison of the DFT optimization cost of the structures obtained by MMFF and R-DSM. DFT optimizations were conducted on 1,000 randomly selected molecules from the QM9 test set using initial structures obtained by MMFF and R-DSM. The number of force calls, total SCF cycles, and SCF time are compared. Statistics were computed for the 964 cases where the initial structures from both MMFF and R-DSM converged to the same final structure.

	# of force calls		# of SCF cycles		SCF time (s)	
	MMFF	R-DSM	MMFF	R-DSM	MMFF	R-DSM
Mean	9.1	4.4	95.4	45.6	1200.0	573.0
Q1	7	3	67	29	850.2	356.4
Q2 (Median)	8	3	87	35	1110.0	472.5
Q3	11	5	114	49	1431.5	643.5

2.5 Application to conformer generation

We applied our R-DSM model to the conformer generation task using the GEOM-QM9 dataset [34]. The GEOM-QM9 dataset provides reference conformations for each molecule, allowing us to evaluate the ability to generate conformations that cover and match these references. R-DSM was trained on a total of 200,000 conformations, comprising 40,000 molecules with 5 selected conformations each, using the same hyperparameters as in the QM9 experiment (see Supplementary Table 4). The test set consists of 200 molecules, each with tens to hundreds of reference conformations. For evaluation, we generated twice as many conformations as those in the reference set, and assessed their quality based on coverage and matching with the reference conformations. The evaluation measurements used were coverage (COV) and matching (MAT), which include recall measurements, COV-R and MAT-R, and precision measurements, COV-P and MAT-P. Further details on the measurements are provided in Section 4.1.

Our approach is designed to refine initial structures; thus, we examine how well R-DSM improves structures by using various types of starting structures and evaluating the refined results. Specifically, we use three types of starting structures obtained from ETKDG [35], ConfGF [24], and GeoDiff [17], respectively. Unlike the prediction task in previous experiments, the evaluation here using recall measurements, COV-R and MAT-R, reflects both accuracy and diversity in combination. Our primary expectation is that R-DSM will enhance the accuracy of each structure, i.e., improving the precision measurements. At the same time, while the generative ability in terms of diversity is highly dependent on the starting structure, we anticipate that refining starting

structures with lower initial accuracy will contribute to improving the recall measurements.

Table 3 Coverage (COV) and matching (MAT) scores of different methods on the GEOM dataset [34]. The precision measurements, COV-P and MAT-P, and the recall measurements, COV-R and MAT-R, are reported as both mean and median values. Two types of initial conformations obtained from ETKDG [35] and GeoDiff [17] are evaluated together with their refinements using MMFF [32] and R-DSM. The threshold δ for the COV scores is set to 0.25 Å.

	COV-P (%) \uparrow		MAT-P (Å) \downarrow		COV-R (%) \uparrow		MAT-R (Å) \downarrow	
	Mean	Median	Mean	Median	Mean	Median	Mean	Median
ETKDG	60.71	66.41	0.2453	0.2302	49.66	48.58	0.2963	0.2917
GeoDiff	35.91	32.00	0.4336	0.4278	67.25	69.01	0.2067	0.2005
ETKDG+MMFF	85.80	95.83	0.1442	0.1202	61.66	63.77	0.2599	0.2360
GeoDiff+MMFF	38.37	36.62	0.4287	0.4202	59.13	60.00	0.2542	0.2485
ETKDG+R-DSM	86.11	93.75	—	0.0887	68.89	68.87	0.1981	0.1808
GeoDiff+R-DSM	38.99	38.20	0.4118	0.4044	70.19	70.83	0.1853	0.1785
ETKDG+MMFF+R-DSM	90.75	98.18	0.0888	0.0622	66.00	68.35	0.2194	0.1934

Table 3 presents the results for two types of initial conformations, each refined using MMFF and our R-DSM model. Additionally, it includes results where ETKDG initial conformations were first refined with MMFF, a commonly used approach for initial guesses in practice, and then further refined with R-DSM. While prior works used a threshold δ of 0.5 Å to show their results, here we compare the COV scores using a reduced threshold of $\delta=0.25$ Å to better assess the improvements from refinement, as discussed in Section 4.1. The full results, including the COV with $\delta=0.5$ Å and the results for ConfGF, can be found in Supplementary Table 1.

Refinement using MMFF improves most measurements, with the exception of recall measurements on GeoDiff generated conformations. In contrast, R-DSM achieves improvements for all initial structures, with more substantial gains on average compared to MMFF. Meanwhile, the mean value of MAT-P of ETKDG+R-DSM is omitted from the table due to the divergence of the values. We observed that very large values of RMSD for certain few predicted structures resulted in divergence of the measurement. Analysis of these cases reveals that divergence occurs when the initial structures are significantly distorted, such as when bond lengths are excessively short, leading to structural collapse (see Supplementary Figure 4). These energetically unfavorable structures prompt R-DSM to predict very high score vectors, resulting in divergence.

For precision measurements, R-DSM shows strong performance, especially when using ETKDG+MMFF as initial structures, achieving significantly lower MAT-P values. This suggests that structures obtained with MMFF may individually exhibit higher accuracy compared to those generated by GeoDiff. On the other hand, recall measurements show the best results for refinements using GeoDiff, indicating that recall is more influenced by the diversity of initial structures. Nevertheless, R-DSM consistently improves accuracy across a variety of initial structures, demonstrating its robustness and adaptability.

Table 4 Mean absolute errors of predicted ensemble properties among different methods. The reported measurements include the average energy (\bar{E}), lowest energy (E_{\min}), average HOMO–LUMO gap ($\bar{\Delta\varepsilon}$), minimum gap ($\Delta\varepsilon_{\min}$), and maximum gap ($\Delta\varepsilon_{\max}$), provided as both mean and median values. Two types of initial conformations obtained from ETKDG [35] and GeoDiff [17] are evaluated together with their refinements using MMFF and R-DSM.

	\bar{E} (kcal/mol)		E_{\min} (kcal/mol)		$\bar{\Delta\varepsilon}$ (eV)		$\Delta\varepsilon_{\min}$ (eV)		$\Delta\varepsilon_{\max}$ (eV)	
	Mean	Median	Mean	Median	Mean	Median	Mean	Median	Mean	Median
ETKDG	21.293	20.556	15.187	15.287	0.3698	0.2947	0.8021	0.5196	0.2359	0.1617
GeoDiff	5.416	2.474	3.157	1.713	0.2808	0.1640	0.7144	0.3020	0.1736	0.0976
ETKDG+MMFF	6.243	2.494	7.220	4.509	0.3175	0.2196	0.3675	0.1634	0.3474	0.2505
GeoDiff+MMFF	6.442	3.000	6.753	4.576	0.2960	0.2243	0.3844	0.2236	0.2771	0.2103
ETKDG+R-DSM	1.250	0.501	0.473	0.199	0.0979	0.0601	0.1969	0.0944	0.0797	0.0346
GeoDiff+R-DSM	1.772	1.004	1.203	0.353	0.1210	0.0698	0.3101	0.1228	0.0973	0.0351
ETKDG+MMFF+R-DSM	2.066	1.610	0.712	0.164	0.1167	0.0951	0.1852	0.1210	0.0970	0.0471

We also evaluated the R-DSM model on an ensemble property benchmark [24], which consists of 30 molecules from the GEOM-QM9 test set, each with multiple conformers. In contrast to the previous evaluation, which focused on measurements based on RMSD, here we assess the accuracy of quantum properties obtained from the predicted structures. For our evaluation, we generated 50 conformers per molecule to assess the accuracy of ensemble properties, following the ensemble error calculation method outlined in previous studies [17, 24]. For the energy, we report the average energy (\bar{E}) and lowest energy (E_{\min}), while for the gap, we consider the average HOMO–LUMO gap ($\bar{\Delta\varepsilon}$), minimum gap ($\Delta\varepsilon_{\min}$), and maximum gap ($\Delta\varepsilon_{\max}$). We used the same types of initial structures as in the GEOM-QM9 experiments.

Table 4 presents the mean absolute errors (MAEs) for the predicted ensemble properties using different methods. The evaluation includes initial conformations generated by ETKDG and GeoDiff, as well as post-refinements using MMFF and R-DSM. Additional performance measures, COV and MAT scores, and results for ConfGF are detailed in Supplementary Table 2. The results indicate that the R-DSM post-refinement significantly improved ensemble property accuracy, in addition to enhancing the structure-based evaluation measurements. Notably, R-DSM demonstrates strong performance in refining ETKDG conformations, approaching chemical accuracy in energies. This highlights R-DSM’s capability to generate conformations with accuracy comparable to quantum chemistry, which is essential for tasks requiring high precision in molecular property predictions.

3 Discussion

The motivation for the development of Riemannian denoising score matching (R-DSM) for molecular structure prediction was driven by the need for more accurate molecular structures in DSM-based prediction and generation. We first considered what constitutes an accurate molecular structure. Accurate in what sense? Our conclusion was that accuracy should be defined in terms of energy. Our approach focused on ensuring accuracy in terms of energy, recognizing that traditional metric like RMSD do not effectively capture the energetic nuances essential to achieving chemical accuracy. To address this,

we employed a physics-informed Riemannian space for the noising/denoising process, which showed a strong correlation between spatial distance and energy differences.

To utilize DSM and R-DSM as optimizers, we reformulated the neural network from a score function to a time-independent form. This approach allows the models to be applied during the inference stage regardless of the predefined noise scheduling and the type of initial structure, making them well-suited for optimization tasks. Consequently, R-DSM has shown consistent improvements in refinement across various types of initial structures in benchmarks with the GEOM-QM9.

Our findings demonstrate that R-DSM can accurately predict equilibrium molecular structures and significantly enhance energy accuracy. Notably, these improvements were achieved without extensive hyperparameter optimization, as we reused hyperparameters from previous the QM9 task for the GEOM-QM9 benchmark. This suggests that further performance gains are possible with additional effort in hyperparameter tuning. Additionally, further advancements could be achieved by optimizing the q -coordinates or Riemannian metric. However, a current limitation of R-DSM is its dependency on an appropriate initial geometry, which restricts its standalone applicability. Future research will aim to mitigate this dependency, enhancing the method’s robustness and utility for a wider range of molecular modeling tasks.

4 Methods

4.1 Measurement details

In this work, to measure the structural deviation, we use four different measurements: RMSD, D-MAE, geodesic distance, and absolute energy difference. This section describes the details of each measurement.

The RMSD is a widely used measurement that measures the average deviation between two structures, \mathcal{C} (reference) and $\hat{\mathcal{C}}$ (predicted), by considering the root mean square of the differences in the atomic positions after optimal alignment using Kabsch algorithm [40]. The RMSD between \mathcal{C} and $\hat{\mathcal{C}}$ is defined as:

$$\text{RMSD}(\mathcal{C}, \hat{\mathcal{C}}) = \sqrt{\frac{1}{N_{\text{atom}}} \sum_{i=1}^{N_{\text{atom}}} \|\mathbf{r}_i - \hat{\mathbf{r}}_i\|_2^2}, \quad (8)$$

where \mathbf{r}_i and $\hat{\mathbf{r}}_i$ are the position vectors of the i -th atom in structures \mathcal{C} and $\hat{\mathcal{C}}$, respectively, and N_{atom} is the number of atoms in each structure.

D-MAE computes the mean absolute deviation in interatomic distances using internal coordinates. The D-MAE between two different structures, \mathcal{C} and $\hat{\mathcal{C}}$, is defined as

$$\text{D-MAE}(\mathcal{C}, \hat{\mathcal{C}}) = \frac{2}{N_{\text{atom}}(N_{\text{atom}} - 1)} \sum_{i < j}^{N_{\text{atom}}} |d_{ij} - \hat{d}_{ij}|, \quad (9)$$

where d_{ij} and \hat{d}_{ij} denote the interatomic distances between the i -th and j -th atoms of \mathcal{C} and $\hat{\mathcal{C}}$, respectively.

The geodesic distance measures the distance between two structures, \mathcal{C} and $\hat{\mathcal{C}}$, on the manifold parameterized by q -coordinates. The geodesic distance is computed using the geodesic interpolation method [30], in which the trajectory connecting \mathcal{C} and $\hat{\mathcal{C}}$ is represented by a discrete series of N images. This trajectory is optimized to become a minimal path, forming a geodesic line. For the optimized trajectory, the geodesic distance is then calculated as the sum of the lengths of the segments $l^{(n)}$, by

$$L = \sum_{n=1}^{N-1} l^{(n)} = \sum_{n=1}^{N-1} \|q^{(n+1)} - q^{(n)}\|_2, \quad (10)$$

where $q^{(n)}$ is the n -th interpolated image between \mathcal{C} and $\hat{\mathcal{C}}$ represented on q -coordinates.

The energy difference was calculated using single-point DFT calculations. Detailed computational settings are provided in Section 4.5.

For the evaluation on conformer generation tasks, we used the COV and MAT scores. The recall versions of these scores are defined as

$$\text{COV-R}(S_{\text{gen}}, S_{\text{ref}}) = \frac{1}{|S_{\text{ref}}|} \left| \left\{ \mathcal{C} \in S_{\text{ref}} \mid \text{RMSD}(\mathcal{C}, \hat{\mathcal{C}}) < \delta, \hat{\mathcal{C}} \in S_{\text{gen}} \right\} \right|, \quad (11)$$

$$\text{MAT-R}(S_{\text{gen}}, S_{\text{ref}}) = \frac{1}{|S_{\text{ref}}|} \sum_{\mathcal{C} \in S_{\text{ref}}} \min_{\hat{\mathcal{C}} \in S_{\text{gen}}} \text{RMSD}(\mathcal{C}, \hat{\mathcal{C}}), \quad (12)$$

where S_{gen} and S_{ref} denote the sets of generated and reference structures, respectively, δ is the threshold criterion, and $|\cdot|$ denotes the number of elements in a given set. The precision versions, COV-P and MAT-P, are defined similarly, with the generated and reference sets swapped in Eq. 11. Note that in these measurements, the RMSD is calculated excluding hydrogen atoms, which is consistent with previous studies.

The COV score depends on the selection of δ ; as δ increases, the COV score also increases. It is therefore important to choose an appropriate threshold to achieve meaningful comparisons. Supplementary Figure 3 presents the RMSD distribution between reference conformations in the GEOM-QM9’s test set, showing that a non-negligible number of conformer pairs are near an RMSD value of 0.5 Å. This suggests that a smaller threshold should be considered to accurately capture variations within closely related conformers. Furthermore, we observe cases where the MAT-R score improves after refinement with the MMFF or Riemannian model at $\delta = 0.5$ Å, but the COV-R score declines at the same threshold. Interestingly, these cases show improvement in COV-R at $\delta = 0.25$ Å. This inconsistency supports the use of a smaller δ to more effectively evaluate refinement-induced improvements. Consequently, we report COV values at the smaller threshold of $\delta = 0.25$ Å and also provide COV

values at $\delta = 0.5 \text{ \AA}$ in Supplementary Table 1 to allow comparison with prior works.

4.2 Formulation of R-DSM

DSM is a widely used method in generative AI applications to learn time-reversed diffusion processes. Consider a diffusion process $(X_t)_{0 \leq t \leq T} \sim \mathbb{P}$ on the Euclidean space that starts from X_0 , representing molecular structures in equilibrium. Without drift term, the process is described by the stochastic differential equation (SDE):

$$dX_t = \beta(t)dB_t, \quad (13)$$

where B_t denotes standard Brownian motion, and $\beta(t)$ denotes noise schedule. The marginal distribution of X_t is a mixture of distributions $\mathbb{P}_t^{(x)} = \mathcal{N}(x, \sigma_t^2 I)$, where x is an equilibrium state structure and $\sigma_t^2 = \int_0^t \beta(s)^2 ds$.

The generation process corresponds to the time-reversed diffusion process $Y_t = X_{T-t}$, which formally follows the SDE:

$$dY_t = \beta(t)^2 \nabla \log p_{T-t}(Y_t) dt + \beta(t) d\tilde{B}_t, \quad (14)$$

where p_t denotes the probability density of X_t . A deep learning model s_θ is employed to approximate the score function $\nabla \log p_t$. By minimizing the loss function

$$\mathcal{L}(\theta) = \mathbb{E}_{\mathbb{P}} \left[\int_0^T w(t) \left\| s_\theta(X_t, t) - \nabla \log p_{t|0}(X_t | X_0) \right\|_2^2 dt \right], \quad (15)$$

we can estimate the score function of the mixture of Gaussian distributions. Here, $w(t)$ is loss weight parameter which is set to σ_t^2 and $p_{t|0}(x_t | x_0)$ is the transition density (or heat kernel), and the gradient operator for the transition density acts on the first variable. The derivative of the transition density is tractable as

$$\nabla p_{t|0}(x_t | x_0) = \frac{x_0 - x_t}{\sigma_t^2}. \quad (16)$$

On an n -dimensional Riemannian manifold (\mathcal{M}, g) , the diffusion process is formulated as

$$dX_t = \beta(t) \sum_{k=1}^n V_k \circ dB_t^k := \beta(t) dB_t^{\mathcal{M}}, \quad (17)$$

where V_k are smooth vector fields on the manifold \mathcal{M} , \circ denotes the Stratonovich integral. The orthonormality of V_k ensures that the diffusion is isotropic with respect to the geometry of the manifold \mathcal{M} , and the stochastic term hereafter simply written as $dB_t^{\mathcal{M}}$.

The time-reversed process is expressed similarly to the Euclidean case:

$$dY_t = \beta^2(t) \nabla_g \log p_{T-t}(Y_t) dt + \beta(t) d\tilde{B}_t^{\mathcal{M}}, \quad (18)$$

where ∇_g is the gradient with respect to the Riemannian metric tensor g . While the score function on a Riemannian manifold can be estimated using the same loss function in Equation (15) with $\|\cdot\|_g^2$, challenges arise because the transition density is generally intractable. Using Varadhan’s asymptotics [38], for small t , the derivative of the transition density can be approximated by the logarithm mapping of the manifold:

$$\nabla_g \log p_{t|0}(x_t|x_0) \approx \frac{1}{\sigma_t^2} \exp_{x_t}^{-1}(x_0). \quad (19)$$

The inverse of the exponential mapping corresponds to the geodesic curve from x_t to x_0 along the tangent vector in $T_{x_t}\mathcal{M}$, which is analogous to $x_0 - x_t$ in Euclidean space.

In implementation, we simulate the diffusion process by sampling velocity vectors in the tangent space $T_{x_t}\mathcal{M}$ corresponding to infinitesimal changes. To ensure isotropic sampling with respect to the Riemannian metric, we define the vector fields V_k to be orthonormal, satisfying $g(V_i, V_j) = \delta_{ij}$. The sampled tangent vectors are mapped back onto the manifold using the exponential map \exp_{x_t} , which solves the geodesic equation with the sampled initial velocity. We numerically solve the second-order differential equation with Levi-Civita connection using the Runge-Kutta method for discretization.

To train s_θ , we used a graph neural network based on the SchNet [41] architecture. Our implementation was primarily based on GeoDiff [17] and TSDiff [18]. For computational efficiency in R-DSM training, we first pretrained R-DSM on noisy structures generated via Euclidean noise-sampling, which can be obtained easily and utilizes an approximated score target. This was followed by fine-tuning using noisy structures generated through Riemannian noise-sampling. Further details are provided in the ‘‘Training details’’ section of Supplementary Information.

4.3 Implementation for molecular structure optimizer

Our primary goal is to optimize sub-optimal molecular structures using DSM. Since the derivative of the transition density is proportional to $x_{\text{optimal}} - x_{\text{sub-optimal}}$ and approximated by s_θ , DSM resembles learning the potential energy gradient [42, 43].

However, conventional diffusion generative modeling starts from pure noise x_T sampled from a prior distribution and obtains x_0 via the time-reversed SDE. This approach is unsuitable when seeking an optimal structure starting from a sub-optimal one, as it does not assume that $x_{\text{sub-optimal}}$ was sampled from a specific time marginal distribution \mathbb{P}_t .

To overcome this, we design the model score function $s_\theta(x_t, t) := f_\theta(x_t)/\sigma_t^2$ using a time-independent neural network f_θ . By setting a small evolution time T , $f_\theta(x_t)$ is crafted to act like a force in the local region of x_{optimal} . This approach reduces coupling between $x_{\text{sub-optimal}}$, a degraded structure of

x_{optimal} , and other equilibrium points x'_{optimal} , resulting $f_{\theta}(x_{\text{sub-optimal}})$ to coincide with $\exp_{x_{\text{sub-optimal}}}^{-1}(x_{\text{optimal}})$.

Based on this insight, we employ a sampling process similar to an ODE-based optimization algorithm [44–46]:

$$dx_{\tau} = \frac{f_{\theta}(x_{\tau})}{1 - \tau} d\tau, \quad (20)$$

where $\tau \in [0, 1]$ is a time-like parameter adopted for scaling f_{θ} and $x_{\tau=0} = x_{\text{sub-optimal}}$. This method is independent of the diffusion time parameter t , eliminating the need to consider from which time marginal distribution \mathbb{P}_t the $x_{\text{sub-optimal}}$ was sampled. Moreover, since f_{θ} is trained on the mixture of Gaussian distributions \mathbb{P}_t , it operates robustly even if $x_{\text{sub-optimal}}$ is generated by methods like MMFF or other generative models.

To implement this ODE sampling, we discretize the equation using Euler’s method:

$$x_{\tau_{i+1}} = \exp_{x_{\tau_i}} \left(\frac{f_{\theta}(x_{\tau_i})}{1 - \tau_i} \Delta\tau \right), \quad (21)$$

where $\Delta\tau$ is the discretization step size, $\tau_i = i\Delta\tau$, and $i = 0, 1, \dots, N - 1$, with N being the total number of steps. Each discretization step computes a tangent vector $v_i = f_{\theta}(x_{\tau_i})\Delta\tau/(1 - \tau_i) \in T_{x_{\tau_i}}\mathcal{M}$, which is then mapped back onto the manifold using the $\exp_{x_{\tau_i}}(v_i)$. This ensures that the updated structures remain on the manifold and adhere to the geometric constraints of the molecular system.

In our experiments, we used 128 discretization steps, meaning that the number of function evaluations equals 128. The effect of the number of evaluation steps on model performance and convergence is presented in Supplementary Figure 5.

4.4 Data

The QM9 dataset [31], derived from the GDB-9 [47] chemical space, is a widely used benchmark in quantum chemistry and molecular machine learning, containing about 133k small organic molecules with up to nine heavy atoms (C, N, O, F). In the QM9 dataset, all molecular geometries are optimized at the B3LYP/6-31G(2df,p) level and the corresponding molecular properties are calculated at the same level. In this study, we used a random split of the QM9 dataset, assigning 100k molecules for training and 10k for testing to evaluate model performance.

In our evaluation on the QM9, we utilize MMFF conformations corresponding to the reference DFT conformations as starting structures for R-DSM and DSM. The MMFF structures are sourced from the QM9_M dataset [33], where each structure is obtained by optimizing the original QM9 geometries using the MMFF [32] with RDKit [48]. The QM9_M dataset has been used in previous studies for property prediction, employing easy-to-obtain MMFF structures in place of computationally demanding DFT structures [49–51].

The GEOM-QM9 dataset is a subset of the GEOM dataset [34] designed to capture the range of accessible 3D conformers for small, neutral molecules with up to nine heavy atoms. GEOM-QM9 provides not only individual 3D conformers for each molecule, but also an ensemble of conformations that reflect the accessible molecular configurations. These conformers were generated with the CREST program [52], which leverages semi-empirical tight-binding DFT (GFN2-xTB) [53] to produce reliable and diverse structures efficiently. Following previous work [17, 24], we assign 40,000 molecules to the training set and 200 molecules to the test set. For each training molecule, we selected five representative conformations, resulting in a total of 200,000 conformations used in training.

4.5 Computational details

We employed quantum chemical calculations to evaluate the energy accuracy. For the QM9 dataset, we used Gaussian 09 [54] to perform single-point and structure optimization calculations with the same computational options as in the original work [31]. Specifically, B3LYP/6-31G(2df,p) DFT was employed with the following options: `opt(calcf, maxstep=5, maxcycles=1000)`, `integral(grid=ultrafine)`, and `scf(maxcycle=200, verytight)`. Each calculation was conducted with four cores on an Intel(R) Xeon(R) CPU E5-2667 v4 @ 3.20GHz node using the `nprocshared=4` option. For the ensemble property evaluation, we utilized the PSI4 toolkit [55] to calculate the energy and HOMO-LUMO gap for each conformer, applying the default computational settings consistent with previous studies [17, 24].

For generation tasks, we used three generative methods: ETKDG [35], ConfGF [24], and GeoDiff [17]. The ETKDG [35] and MMFF [32] algorithms, implemented in RDKit [48] (version 2020.09.1), were used. We also employed pretrained ConfGF and GeoDiff models, obtained from their respective repositories at <https://github.com/DeepGraphLearning/ConfGF> and <https://github.com/MinkaiXu/GeoDiff/tree/pretrain>.

5 Data availability

The QM9 dataset [31] is accessible at <https://doi.org/10.1038/s41597-022-01288-4>. The QM9_M dataset [33], which includes MMFF structures corresponding to QM9 structures, is available at <https://doi.org/10.1021/acs.jctc.9b00001>. We used the GEOM [34] dataset, preprocessed and available at <https://github.com/MinkaiXu/GeoDiff/tree/pretrain>.

6 Code availability

An implementation of the proposed model, R-DSM, will be made available.

References

- [1] Jorgensen, W.L.: The many roles of computation in drug discovery. *Science* **303**(5665), 1813–1818 (2004)
- [2] Jain, A., Ong, S.P., Hautier, G., Chen, W., Richards, W.D., Dacek, S., Cholia, S., Gunter, D., Skinner, D., Ceder, G., et al.: Commentary: The materials project: A materials genome approach to accelerating materials innovation. *APL materials* **1**(1) (2013)
- [3] Cramer, C.J.: *Essentials of Computational Chemistry: Theories and Models*. John Wiley & Sons, Hoboken, NJ, USA (2013)
- [4] Leach, A.R.: *Molecular Modelling: Principles and Applications*. Pearson education, Harlow, England (2001)
- [5] Jones, R.O.: Density functional theory: Its origins, rise to prominence, and future. *Reviews of modern physics* **87**(3), 897–923 (2015)
- [6] Parr, R.G., Weitao, Y.: *Density-Functional Theory of Atoms and Molecules*. Oxford University Press, New York, USA (1995)
- [7] Friesner, R.A.: Ab initio quantum chemistry: Methodology and applications. *Proceedings of the National Academy of Sciences* **102**(19), 6648–6653 (2005)
- [8] Bowler, D.R., Miyazaki, T.: *Methods in electronic structure calculations*. *Reports on Progress in Physics* **75**(3), 036503 (2012)
- [9] Goedecker, S.: Linear scaling electronic structure methods. *Reviews of Modern Physics* **71**(4), 1085 (1999)
- [10] Woo, J., Kim, W.Y., Choi, S.: System-specific separable basis based on tucker decomposition: Application to density functional calculations. *Journal of chemical theory and computation* **18**(5), 2875–2884 (2022)
- [11] Rupp, M., Tkatchenko, A., Müller, K.-R., Von Lilienfeld, O.A.: Fast and accurate modeling of molecular atomization energies with machine learning. *Physical review letters* **108**(5), 058301 (2012)
- [12] Butler, K.T., Davies, D.W., Cartwright, H., Isayev, O., Walsh, A.: Machine learning for molecular and materials science. *Nature* **559**(7715), 547–555 (2018)
- [13] Von Lilienfeld, O.A.: Quantum machine learning in chemical compound space. *Angewandte Chemie International Edition* **57**(16), 4164–4169 (2018)

- [14] Woo, J., Kim, S., Kim, W.Y.: Dynamic precision approach for accelerating large-scale eigenvalue solvers in electronic structure calculations on graphics processing units. *Journal of Chemical Theory and Computation* **19**(5), 1457–1465 (2023)
- [15] Woo, J., Youn Kim, W., Choi, S.: Efficient shift-and-invert preconditioning for multi-gpu accelerated density functional calculations. *Journal of Chemical Theory and Computation* **20**(17), 7443–7452 (2024)
- [16] Smith, J.S., Isayev, O., Roitberg, A.E.: Ani-1: an extensible neural network potential with dft accuracy at force field computational cost. *Chemical science* **8**(4), 3192–3203 (2017)
- [17] Xu, M., Yu, L., Song, Y., Shi, C., Ermon, S., Tang, J.: GeoDiff: a Geometric Diffusion Model for Molecular Conformation Generation. *arXiv* (2022)
- [18] Kim, S., Woo, J., Kim, W.Y.: Diffusion-based generative ai for exploring transition states from 2d molecular graphs. *Nature Communications* **15**(1), 341 (2024)
- [19] Dral, P.O., Owens, A., Dral, A., Csányi, G.: Hierarchical machine learning of potential energy surfaces. *The Journal of Chemical Physics* **152**(20) (2020)
- [20] Chmiela, S., Sauceda, H.E., Müller, K.-R., Tkatchenko, A.: Towards exact molecular dynamics simulations with machine-learned force fields. *Nature communications* **9**(1), 3887 (2018)
- [21] Behler, J., Parrinello, M.: Generalized neural-network representation of high-dimensional potential-energy surfaces. *Physical review letters* **98**(14), 146401 (2007)
- [22] Xu, M., Wang, W., Luo, S., Shi, C., Bengio, Y., Gomez-Bombarelli, R., Tang, J.: An end-to-end framework for molecular conformation generation via bilevel programming. In: *International Conference on Machine Learning*, pp. 11537–11547 (2021). PMLR
- [23] Mansimov, E., Mahmood, O., Kang, S., Cho, K.: Molecular geometry prediction using a deep generative graph neural network. *Scientific reports* **9**(1), 20381 (2019)
- [24] Shi, C., Luo, S., Xu, M., Tang, J.: Learning Gradient Fields for Molecular Conformation Generation. *arXiv* (2021)
- [25] Luo, S., Shi, C., Xu, M., Tang, J.: Predicting molecular conformation via dynamic graph score matching. *Advances in Neural Information*

Processing Systems **34**, 19784–19795 (2021)

- [26] Zhang, H., Li, S., Zhang, J., Wang, Z., Wang, J., Jiang, D., Bian, Z., Zhang, Y., Deng, Y., Song, J., *et al.*: Sdegen: learning to evolve molecular conformations from thermodynamic noise for conformation generation. *Chemical Science* **14**(6), 1557–1568 (2023)
- [27] Zhu, J., Xia, Y., Liu, C., Wu, L., Xie, S., Wang, Y., Wang, T., Qin, T., Zhou, W., Li, H., *et al.*: Direct molecular conformation generation. arXiv preprint arXiv:2202.01356 (2022)
- [28] Duan, C., Du, Y., Jia, H., Kulik, H.J.: Accurate transition state generation with an object-aware equivariant elementary reaction diffusion model. *Nature Computational Science* **3**(12), 1045–1055 (2023)
- [29] Simm, G.N., Hernández-Lobato, J.M.: A generative model for molecular distance geometry. arXiv preprint arXiv:1909.11459 (2019)
- [30] Zhu, X., Thompson, K.C., Martínez, T.J.: Geodesic interpolation for reaction pathways. *The Journal of Chemical Physics* **150**(16) (2019)
- [31] Ramakrishnan, R., Dral, P.O., Rupp, M., Von Lilienfeld, O.A.: Quantum chemistry structures and properties of 134 kilo molecules. *Scientific data* **1**(1), 1–7 (2014)
- [32] Halgren, T.A.: Merck molecular force field. i. basis, form, scope, parameterization, and performance of mmff94. *Journal of computational chemistry* **17**(5-6), 490–519 (1996)
- [33] Lu, J., Wang, C., Zhang, Y.: Predicting molecular energy using force-field optimized geometries and atomic vector representations learned from an improved deep tensor neural network. *Journal of chemical theory and computation* **15**(7), 4113–4121 (2019)
- [34] Axelrod, S., Gomez-Bombarelli, R.: Geom, energy-annotated molecular conformations for property prediction and molecular generation. *Scientific Data* **9**(1), 185 (2022)
- [35] Riniker, S., Landrum, G.A.: Better informed distance geometry: using what we know to improve conformation generation. *Journal of chemical information and modeling* **55**(12), 2562–2574 (2015)
- [36] Nash, J.: The imbedding problem for riemannian manifolds. *Annals of mathematics* **63**(1), 20–63 (1956)
- [37] Tachibana, A., Fukui, K.: Intrinsic field theory of chemical reactions. *Theoretica chimica acta* **51**, 275–296 (1979)

- [38] Varadhan, S.S.: Asymptotic probabilities and differential equations. *Communications on Pure and Applied Mathematics* **19**(3), 261–286 (1966)
- [39] Janet, J.P., Duan, C., Yang, T., Nandy, A., Kulik, H.J.: A quantitative uncertainty metric controls error in neural network-driven chemical discovery. *Chemical science* **10**(34), 7913–7922 (2019)
- [40] Kabsch, W.: A solution for the best rotation to relate two sets of vectors. *Acta Crystallographica Section A: Crystal Physics, Diffraction, Theoretical and General Crystallography* **32**(5), 922–923 (1976)
- [41] Schütt, K., Kindermans, P.-J., Saucedo Felix, H.E., Chmiela, S., Tkatchenko, A., Müller, K.-R.: SchNet: A continuous-filter convolutional neural network for modeling quantum interactions. *Advances in neural information processing systems* **30** (2017)
- [42] Feng, S., Ni, Y., Lan, Y., Ma, Z.-M., Ma, W.-Y.: Fractional denoising for 3d molecular pre-training. In: *International Conference on Machine Learning*, pp. 9938–9961 (2023). PMLR
- [43] Zaidi, S., Schaarschmidt, M., Martens, J., Kim, H., Teh, Y.W., Sanchez-Gonzalez, A., Battaglia, P., Pascanu, R., Godwin, J.: Pre-training via denoising for molecular property prediction. *arXiv preprint arXiv:2206.00133* (2022)
- [44] Chen, R.T., Lipman, Y.: Riemannian flow matching on general geometries. *arXiv preprint arXiv:2302.03660* (2023)
- [45] Tong, A., Fatras, K., Malkin, N., Huguet, G., Zhang, Y., Rector-Brooks, J., Wolf, G., Bengio, Y.: Improving and generalizing flow-based generative models with minibatch optimal transport. *arXiv preprint arXiv:2302.00482* (2023)
- [46] Lipman, Y., Chen, R.T., Ben-Hamu, H., Nickel, M., Le, M.: Flow matching for generative modeling. *arXiv preprint arXiv:2210.02747* (2022)
- [47] Ruddigkeit, L., Van Deursen, R., Blum, L.C., Reymond, J.-L.: Enumeration of 166 billion organic small molecules in the chemical universe database gdb-17. *Journal of chemical information and modeling* **52**(11), 2864–2875 (2012)
- [48] Landrum, G., et al.: RDKit: Open-source cheminformatics. *Zenodo* (2006)
- [49] Kim, H., Woo, J., Kim, S., Moon, S., Kim, J.H., Kim, W.Y.: Geotmi: predicting quantum chemical property with easy-to-obtain geometry via positional denoising. *Advances in Neural Information Processing Systems*

36 (2024)

- [50] Lu, J., Xia, S., Lu, J., Zhang, Y.: Dataset construction to explore chemical space with 3d geometry and deep learning. *Journal of chemical information and modeling* **61**(3), 1095–1104 (2021)
- [51] Pinheiro, G.A., Da Silva, J.L., Quiles, M.G.: Smiclr: contrastive learning on multiple molecular representations for semisupervised and unsupervised representation learning. *Journal of Chemical Information and Modeling* **62**(17), 3948–3960 (2022)
- [52] Pracht, P., Bohle, F., Grimme, S.: Automated exploration of the low-energy chemical space with fast quantum chemical methods. *Physical Chemistry Chemical Physics* **22**(14), 7169–7192 (2020)
- [53] Bannwarth, C., Ehlert, S., Grimme, S.: Gfn2-xtb—an accurate and broadly parametrized self-consistent tight-binding quantum chemical method with multipole electrostatics and density-dependent dispersion contributions. *Journal of chemical theory and computation* **15**(3), 1652–1671 (2019)
- [54] Frisch, M.J., Trucks, G.W., Schlegel, H.B., Scuseria, G.E., Robb, M.A., Cheeseman, J.R., Scalmani, G., Barone, V., Mennucci, B., Petersson, G.A., Nakatsuji, H., Caricato, M., Li, X., Hratchian, H.P., Izmaylov, A.F., Bloino, J., Zheng, G., Sonnenberg, J.L., Hada, M., Ehara, M., Toyota, K., Fukuda, R., Hasegawa, J., Ishida, M., Nakajima, T., Honda, Y., Kitao, O., Nakai, H., Vreven, T., Montgomery, J.A., Peralta, J.E., Ogliaro, F., Bearpark, M., Heyd, J.J., Brothers, E., Kudin, K.N., Staroverov, V.N., Kobayashi, R., Normand, J., Raghavachari, K., Rendell, A., Burant, J.C., Iyengar, S.S., Tomasi, J., Cossi, M., Rega, N., Millam, J.M., Klene, M., Knox, J.E., Cross, J.B., Bakken, V., Adamo, C., Jaramillo, J., Gomperts, R., Stratmann, R.E., Yazyev, O., Austin, A.J., Cammi, R., Pomelli, C., Ochterski, J.W., Martin, R.L., Morokuma, K., Zakrzewski, V.G., Voth, G.A., Salvador, P., Dannenberg, J.J., Dapprich, S., Daniels, A.D., Farkas, Ö., Foresman, J.B., Ortiz, J.V., Cioslowski, J., Fox, D.J.: *Gaussian 09 Revision A.2* (2009)
- [55] Smith, D.G., Burns, L.A., Simmonett, A.C., Parrish, R.M., Schieber, M.C., Galvelis, R., Kraus, P., Kruse, H., Di Remigio, R., Alenaizan, A., et al.: Psi4 1.4: Open-source software for high-throughput quantum chemistry. *The Journal of chemical physics* **152**(18) (2020)

7 Acknowledgments

8 Author information

These authors contributed equally: Jeheon Woo, Seonghwan Kim.

8.1 Authors and affiliations

Department of Chemistry, KAIST, Daejeon, Republic of Korea.

Jeheon Woo, Seonghwan Kim, Jun Hyeong Kim, Woo Youn Kim

AI Institute, KAIST, Daejeon, Republic of Korea.

Woo Youn Kim

8.2 Contributions

J. Woo and S. Kim contributed equally to this work. They designed the methodology and the experiments. J. H. Kim performed the conformer generation experiments. All authors wrote the manuscript together, and W. Y. Kim supervised the project.

8.3 Corresponding author

Correspondence to Woo Youn Kim.

9 Competing interests

The authors declare no competing interests.

Supplementary Information for:
**Riemannian Denoising Score Matching for Molecular
Structure Optimization with Accurate Energy**

Jeheon Woo,^{1†} Seonghwan Kim,^{1†} Jun Hyeong Kim,¹ and Woo Youn Kim^{1,2*}

¹*Department of Chemistry, KAIST, 291 Daehak-ro, Yuseong-gu, 34141, Daejeon, Republic of Korea.*

²*AI Institute, KAIST, 291 Daehak-ro, Yuseong-gu, 34141, Daejeon, Republic of Korea.*

*Corresponding author. E-mail: wooyoun@kaist.ac.kr

Contributing authors: woojh@kaist.ac.kr; dmdtk00@kaist.ac.kr; junhkim1226@kaist.ac.kr

[†]*These authors contributed equally to this work.*

1 Supplementary results

Supplementary Table 1: **Coverage (COV) and matching (MAT) scores of different methods on the GEOM-QM19 dataset [1].** The recall measurements, COV-R and MAT-R, and the precision measurements, COV-P and MAT-P, are reported as both mean and median values. Three types of initial conformations obtained from ETKDG [2], ConfGF [3], and GeoDiff [4] are evaluated together with their refinements using MMFF and R-DSM.

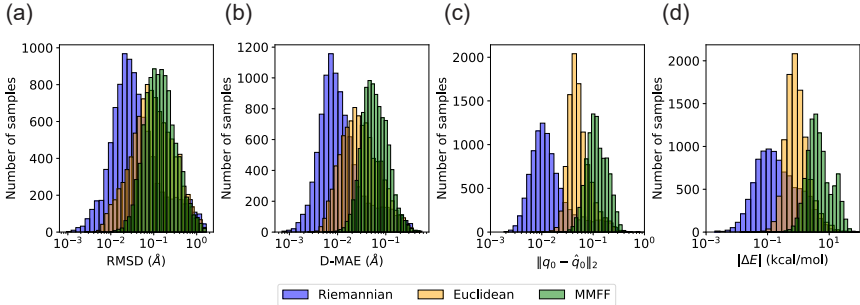
	COV-R ^{0=0.5} (%)		COV-R ^{0=0.25} (%)		MAT-R (A)		COV-P ^{0=0.5} (%)		COV-P ^{0=0.25} (%)		MAT-P (A)	
	Mean	Median	Mean	Median	Mean	Median	Mean	Median	Mean	Median	Mean	Median
ETKDG	84.00	92.06	49.66	48.58	0.2963	0.2917	92.51	98.66	60.71	66.41	0.2453	0.2302
ConfGF	89.71	94.35	52.62	50.45	0.2675	0.2721	46.50	42.62	21.65	17.55	0.5135	0.5102
GeoDiff	90.52	94.34	67.25	69.01	0.2067	0.2005	52.99	51.56	35.91	32.00	0.4336	0.4278
ETKDG+MMFF	81.92	88.52	61.66	63.77	0.2599	0.2360	95.51	100.00	85.80	95.83	0.1442	0.1202
ConfGF+MMFF	86.44	90.42	60.94	60.66	0.2456	0.2400	54.74	50.83	39.11	37.74	0.4260	0.4238
GeoDiff+MMFF	85.13	89.18	59.13	60.00	0.2542	0.2485	53.76	51.25	38.37	36.62	0.4287	0.4202
ETKDG+R-DSM	87.18	93.10	68.89	68.87	0.1981	0.1808	95.15	100.00	86.11	93.75	—	0.0887
ConfGF+R-DSM	92.38	95.27	70.59	73.24	0.1841	0.1760	52.39	49.54	35.32	30.47	—	—
GeoDiff+R-DSM	90.46	94.04	70.19	70.83	0.1853	0.1785	53.98	51.66	38.99	38.20	0.4118	0.4044
ETKDG+MMFF+R-DSM	83.43	90.38	66.00	68.35	0.2194	0.1934	96.35	100.00	90.75	98.18	0.0888	0.0622

Supplementary Table 2: **Coverage (COV) and matching (MAT) scores of different methods on the ensemble property test set.** The recall measurements, COV-R and MAT-R, and the precision measurements, COV-P and MAT-P, are reported as both mean and median values. Three types of initial conformations obtained from ETKDG [2], ConfGF [3], and GeoDiff [4] are evaluated together with their refinements using MMFF and R-DSM.

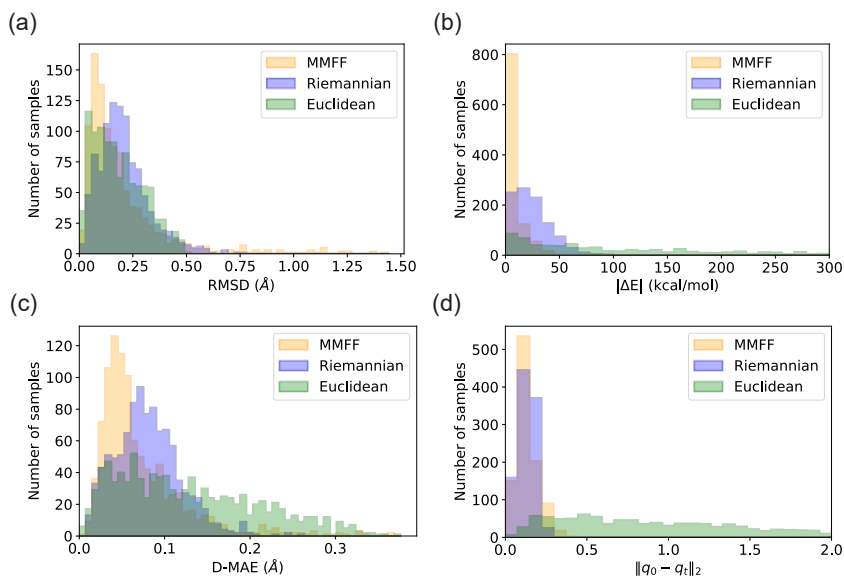
	COV-R ^{ensemble} (%)		COV-R ^{ensemble} (%)		MAT-R (Å)		COV-P ^{ensemble} (%)		MAT-P (Å)			
	Mean	Median	Mean	Median	Mean	Median	Mean	Median	Mean	Median		
ETKDG	86.89	100.00	70.04	86.67	0.2354	0.1596	91.38	100.00	62.62	72	0.2511	0.2057
ConfGF	90.75	100.00	72.67	83.97	0.1965	0.1558	46.33	38.00	24.60	22	0.5757	0.5144
GeoDiff	94.80	100.00	73.48	71.43	0.1663	0.1447	48.07	44.00	27.80	22	0.5454	0.4721
ETKDG+MMFF	85.98	100.00	70.20	77.78	0.2465	0.2012	92.00	100.00	80.28	96	0.1924	0.1677
ConfGF+MMFF	88.15	100.00	68.16	73.08	0.2351	0.2063	50.07	38.00	35.20	31	0.5251	0.4889
GeoDiff+MMFF	86.19	100.00	65.10	69.05	0.2432	0.2133	47.73	44.00	32.80	26	0.5324	0.4899
ETKDG+R-DSM	89.69	100.00	80.58	100.00	0.1514	0.0649	92.83	100.00	84.14	98	0.1404	0.0744
ConfGF+R-DSM	83.27	100.00	62.02	64.58	0.2347	0.2132	51.54	40.83	34.78	28	–	0.4984
GeoDiff+R-DSM	96.30	100.00	80.19	87.08	0.1346	0.1066	49.40	44.00	33.87	27	–	0.4597
ETKDG+MMFF+R-DSM	85.48	100.00	74.62	86.67	0.1925	0.1279	92.07	100.00	86.07	100	0.1286	0.0605

Supplementary Table 3: **Comparison of RMSD, D-MAE, and norm distance at q -coordinates for different models on the QM9 [5] test set.** This table shows root mean square deviation (RMSD), mean absolute error of interatomic distances (D-MAE), and norm distance at q -coordinates for the predicted structures by MMFF, DSM, R-DSM, and R-DSM*. R-DSM* refers to the R-DSM model trained only on noisy structures generated by Euclidean noise-sampling.

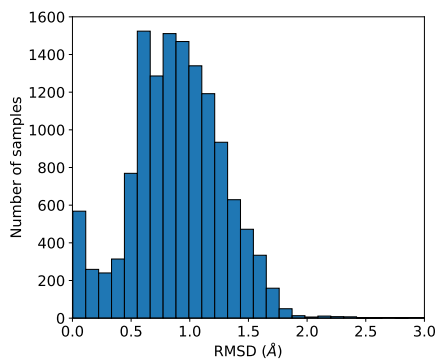
	RMSD (Å)		D-MAE (Å)		$\ q_0 - \hat{q}_0\ _2$	
	Mean	Median	Mean	Median	Mean	Median
MMFF	0.200	0.137	0.0717	0.0571	0.131	0.115
DSM	0.166	0.091	0.0454	0.0280	0.0612	0.0487
R-DSM	0.104	0.031	0.0256	0.0095	0.0269	0.0119
R-DSM*	0.162	0.087	0.0435	0.0257	0.0440	0.0286



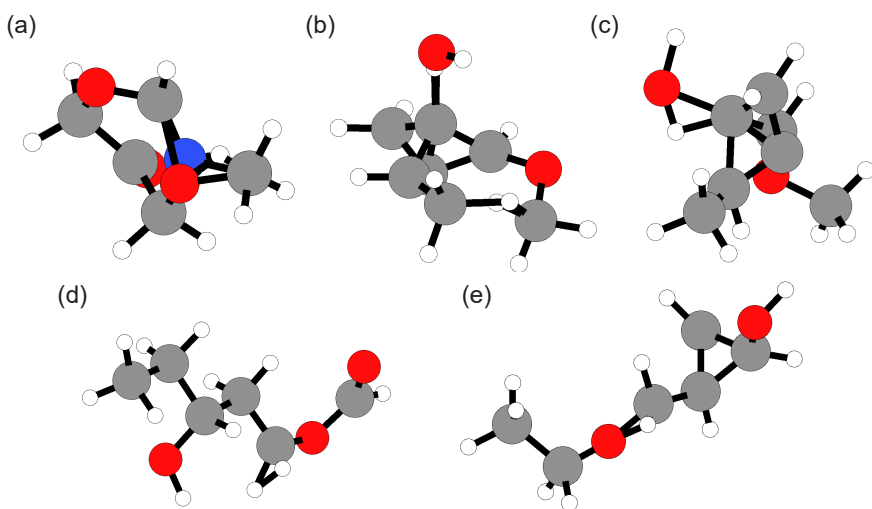
Supplementary Figure 1: **Comparative analysis of molecular structures predicted by R-DSM, DSM, and MMFF.** Histograms compare the distributions of (a) root mean square deviation (RMSD), (b) mean absolute error of interatomic distances (D-MAE), and (c) norm distance at q -coordinates, and (d) absolute energy difference ($|\Delta E|$); predicted by R-DSM (blue) and DSM (yellow) models and MMFF (green). The sampling was performed on the QM9 [5] set, and the energy values were obtained from single point DFT calculations.



Supplementary Figure 2: **Comparison of molecular structures sampled from noisy distributions of Euclidean and Riemannian spaces.** The distributions of (a) RMSD, (b) absolute energy difference $|\Delta E|$, (c) mean absolute error of interatomic distances (D-MAE), and (d) norm distance at q -coordinates; for molecular structures obtained by MMFF (orange), Riemannian noise-sampling (blue), and Euclidean noise-sampling (green), with the DFT structures as reference. Each distribution is plotted with 1,000 randomly selected molecules for each method; however, 23 samples are excluded from the Euclidean noise-sampled structures due to failure to converge in the SCF calculation.



Supplementary Figure 3: **Distribution of RMSD between reference conformations of the GEOM-QM9 [1] test set.**



Supplementary Figure 4: **Visualization of starting structures diverged in refinement using R-DSM.** (a) and (b) show the starting structures obtained by ConfGF, while (c) presents the starting structure from GeoDiff. (d) and (e) show the starting structures from ETKDG. Extremely short bond lengths or collapsing structures can be observed.

2 Training details

This section outlines the training details for R-DSM. The loss function of R-DSM is defined as:

$$\mathcal{L}(\theta) = \mathbb{E}_{\mathcal{P}} \left[\int_0^{t_{\max}} \sigma_t^2 \left\| s_{\theta}(X_t, t) - \frac{\exp_{X_t}^{-1}(X_0)}{\sigma_t^2} \right\|_g^2 dt \right]. \quad (1)$$

By reformulating s_{θ} with f_{θ}/σ_t^2 , Eq. 1 becomes

$$\mathcal{L}(\theta) = \mathbb{E}_{\mathcal{P}} \left[\int_0^{t_{\max}} \frac{1}{\sigma_t^2} \left\| f_{\theta}(X_t) - \exp_{X_t}^{-1}(X_0) \right\|_g^2 dt \right]. \quad (2)$$

Thus, the neural network $f_{\theta}(X_t)$ is trained to predict $\exp_{X_t}^{-1}(X_0)$, the direction vector on the tangent plane.

To train the R-DSM model efficiently, we adopted a two-step approach. Initially, R-DSM was pretrained using noisy structures generated through Euclidean noise-sampling, which can be obtained immediately. This was followed by fine-tuning using noisy structures obtained from Riemannian noise-sampling.

During pretraining, we approximate the logarithmic map $\exp_{x_t}^{-1}(x_0)$ for computational efficiency as follows:

$$\exp_{x_t}^{-1}(x_0) \approx \frac{\text{Proj}_{T_{x_t}\mathcal{M}}(q_0 - q_t)}{\|\text{Proj}_{T_{x_t}\mathcal{M}}(q_0 - q_t)\|_2} \|q_0 - q_t\|_2, \quad (3)$$

where q_t and q_0 denotes the vector of q -coordinate in $\mathbb{R}^{|\mathcal{E}|}$ corresponding to x_t and x_0 , respectively, and $\text{Proj}_{T_{x_t}\mathcal{M}}$ represents the projection of $(q_0 - q_t)$ onto the tangent plane at q_t which is subspace of $\mathbb{R}^{|\mathcal{E}|}$. The size relationship among the three vectors is as follows: $\|\exp_{x_t}^{-1}(x_0)\|_g \geq \|q_0 - q_t\|_2 \geq \|\text{Proj}_{T_{x_t}\mathcal{M}}(q_0 - q_t)\|_2$. To correct the reduction in length due to projection, we rescale the vector to match $\|q_0 - q_t\|_2$. Accurately computing $\exp_{x_t}^{-1}(x_0)$, by determining the geodesic path between x_0 and x_t on the manifold and obtaining the associated tangent vector, involves a non-negligible computational cost. For efficiency, this approximation is applied instead.

As described in the main text, the noisy structure x_t in Riemannian space is obtained as follows:

$$x_t = \exp_{x_0}(\sigma_t \varepsilon_t), \quad (4)$$

where $\varepsilon_t \in T_{x_0}\mathcal{M}$ is a tangent vector representing the direction of noise. In our implementation, the diffusion process is simulated by sampling velocity vectors within the tangent space $T_{x_t}\mathcal{M}$ to represent small incremental changes. These sampled tangent vectors are then mapped back onto the manifold via the exponential map \exp_{x_t} , effectively solving the geodesic equation with the initial velocity provided by the sample. We use the Runge-Kutta method to discretize and solve Eq. 4 numerically. For efficiency, noisy structures were pre-generated and stored for use in the training phase, with three noisy structures for each reference structure in QM9 [5] and one for each in GEOM-QM9 [1].

Details on hyperparameters related to DSM and R-DSM can be found in Supplementary Table 4.

Supplementary Table 4: **Hyperparameters of R-DSM and DSM.**

parameter	R-DSM	DSM
β_1	1e-7	1e-7
β_T	2e-3	2e-3
β scheduler	sigmoid	sigmoid
T	5,000	5,000
t_{\max}	1,500	5,000
hidden dimension	128	128
layers	7	7
activation	swish	swish
batch size	300	300
epoch	3,000	3,000
sampling method	ODE	ODE
sampling steps	128	128

3 Performance and the number of function evaluations

This section examines the performance of DSM and R-DSM models in terms of convergence of accuracy and computational efficiency as a function of the number of function evaluations (nfe).

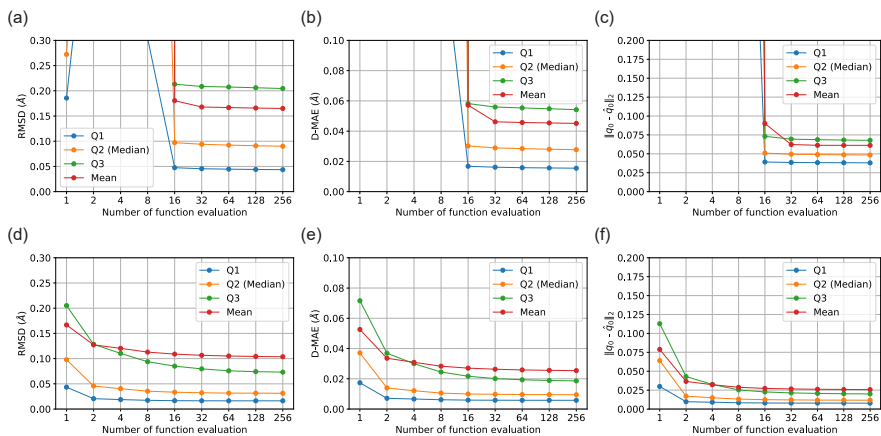
In Supplementary Figure 5, convergence of accuracy is analyzed by plotting various measurements (RMSD, D-MAE, and $\|q_0 - \hat{q}_0\|_2$) as a function of nfe. R-DSM[†] demonstrates stable accuracy even at low nfe values, indicating that the model maintains robustness with fewer function evaluations. Both DSM and R-DSM[†] converge across all three measurements by nfe=128.

Compared to DSM, R-DSM[†] requires exponential mapping, which introduces additional computational cost. Given the trade-off between performance convergence and inference time, selecting an appropriate nfe is crucial for efficiency. When nfe is sufficiently large, the denoising of molecular structures on the manifold can be approximated in smaller, linear segments, allowing the tangent vectors to be applied in Euclidean space without the need for exponential mapping.

To explore this further, we evaluate R-DSM without exponential mapping at nfe=16 and 128, comparing its accuracy and computational efficiency with R-DSM[†] (see Supplementary Table 5). The results show that R-DSM achieves nearly equivalent performance to R-DSM[†] at nfe=128, while being approximately five times faster. Therefore, in evaluations in the main text, we used DSM and R-DSM with nfe=128.

Supplementary Table 5: **Elapsed CPU time per sample and comparison of RMSD, D-MAE, and norm distance at q -coordinates for DSM and R-DSM models with the number of function evaluations (nfe) of 16 and 128.** Sampling for the two R-DSM models was performed both with and without exponential mapping, referred to as R-DSM[†] and R-DSM, respectively. This table shows the root mean square deviation (RMSD), mean absolute error of interatomic distances (D-MAE), and norm distance at q -coordinates ($\|q_0 - \hat{q}_0\|_2$) for the predicted structures by DSM, R-DSM, and R-DSM[†] at two different levels of function evaluations. Elapsed times were measured using 16 threads on a computing node equipped with Intel(R) Xeon(R) Gold 6326 CPUs (2.90 GHz) and a batch size of 300.

Method	RMSD (Å)		D-MAE (Å)		$\ q_0 - \hat{q}_0\ _2$		Time
	Mean	Median	Mean	Median	Mean	Median	
DSM (nfe=16)	0.180	0.0971	0.0572	0.0302	0.0901	0.0510	0.046 s
R-DSM [†] (nfe=16)	0.109	0.0334	0.0270	0.00996	0.0273	0.0124	0.31 s
R-DSM (nfe=16)	0.109	0.0335	0.0270	0.00999	0.0299	0.0130	0.070 s
DSM (nfe=128)	0.166	0.0911	0.0454	0.0280	0.0612	0.0487	0.32 s
R-DSM [†] (nfe=128)	0.104	0.0315	0.0256	0.00952	0.0259	0.0118	2.40 s
R-DSM (nfe=128)	0.104	0.0314	0.0256	0.00951	0.0269	0.0119	0.55 s



Supplementary Figure 5: **Convergence analysis of different measurements based on the number of function evaluations.** (a)-(c) represent results obtained from DSM, while (d)-(f) correspond to R-DSM[†] with exponential mapping. The measurements plotted include root mean square deviation (RMSD), mean absolute error of interatomic distances (D-MAE), and norm distance as a function of the number of function evaluations. Each subfigure shows the distribution of performance across different quartiles (Q1, Q2, Q3) and the mean.

Supplementary References

- [1] S. Axelrod and R. Gomez-Bombarelli, "Geom, energy-annotated molecular conformations for property prediction and molecular generation," *Scientific Data* **9**, 185 (2022).
- [2] S. Riniker and G. A. Landrum, "Better informed distance geometry: using what we know to improve conformation generation," *Journal of chemical information and modeling* **55**, 2562–2574 (2015).
- [3] C. Shi, S. Luo, M. Xu, and J. Tang, "Learning gradient fields for molecular conformation generation," (2021).
- [4] M. Xu, L. Yu, Y. Song, C. Shi, S. Ermon, and J. Tang, "Geodiff: a geometric diffusion model for molecular conformation generation," (2022).
- [5] R. Ramakrishnan, P. O. Dral, M. Rupp, and O. A. Von Lilienfeld, "Quantum chemistry structures and properties of 134 kilo molecules," *Scientific data* **1**, 1–7 (2014).